

On the Impact of an Integrated HIP Treatment on the Very High Cycle Fatigue Life of Ni-Based SX Superalloys



LUCIANA MARIA BORTOLUCI ORMASTRONI, INMACULADA LOPEZ-GALILEA, BENJAMIN RUTTERT, SEBASTIAN WEBER, FLORENT MAUGET, PATRICK VILLECHAISE, and JONATHAN CORMIER

The influence of an integrated hot isostatic pressing (HIP) treatment was investigated for two single-crystalline nickel-based superalloys under very high cycle fatigue at 1000 °C in fully reversed conditions ($R_e = -1$). The fatigue life is improved significantly by performing heat-treatments within the HIP unit. The HIP-compacted pore morphology and its impact on the crack initiation is considered as well. The HIPed specimens fail at low-angle grain boundary structures that have developed around the compacted casting pores.

<https://doi.org/10.1007/s11661-022-06882-0>

© The Minerals, Metals & Materials Society and ASM International 2022

I. INTRODUCTION

AMONG the harshest environments that materials can withstand, the turbine section of an aircraft engine is the most severe.^[1] During the past years, nickel-based superalloys in single-crystalline (SX) form have been successfully used as material for blade and vane application, especially in the hottest sections of the gas turbine^[2,3] suffering damages such as creep, hot corrosion, and oxidation.^[3-5] In the past decades, the improvement of superalloys chemistry, casting processes, and the more efficient design for air-cooling systems increased the operational temperature.^[1,6] However, the casting process and the standard heat treatments result in the unavoidable presence of metallurgical defects such as pores, eutectics, and incipient melting (IM).^[2,6-8] Incipient melting is the unintentional re-melting during heat-treatment of the eutectic phase that exhibits the lowest melting temperature in the system.

During service, components made of superalloys may experience small localized plastic strain (*i.e.* low frequency cyclic loading) or vibrations and airflow between the stages of the turbine (*i.e.* very high frequency cyclic loading).^[2,3] The porosity introduced during SX solidification (casting-porosity) is responsible for the majority of crack initiation events/failure cases of cycling loading in cast superalloys.^[9-17] The casting pores size can be decreased and even suppressed by applying a hot isostatic pressing (HIP) treatment. This technology involves the simultaneous application of isostatic pressure and elevated temperature to a component / sample.^[18] From an industrial standpoint, HIP treatments are generally applied as an additional treatment step to the necessary (stepwise) solution annealing and precipitation hardening treatments.

Ni-based SX superalloys are usually HIPed at temperatures higher than gamma prime (γ') solvus under remarkably high pressure, bearing the risk of recrystallization (RX) and IM. The employed pressure medium is usually an inert gas such as argon (Ar) pressurized up to 200 MPa.^[19] The parameters of the industrial HIP (temperature, pressure and duration) have to be carefully optimized under the conditions of complete pore annihilation, avoiding RX, IM and minimizing processing costs.^[20] Recent studies have shown the benefits of incorporating the solution annealing heat treatment into the HIP process with respect to mechanical properties such as creep and fatigue.^[21,22] This new type of heat treatment, known as integrated HIP heat treatment or high-pressure heat treatment, is applied in the present study to two Ni-based SX superalloys of type ERBO/1 and CMSX-4 Plus. These superalloys were chosen as they are either widely used for aero-engines applications

LUCIANA MARIA BORTOLUCI ORMASTRONI, FLORENT MAUGET, PATRICK VILLECHAISE, and JONATHAN CORMIER are with the Institut Pprime, UPR CNRS 3346, Physics and Mechanics of Materials Department, ISAE-ENSMA, 1 avenue Clément Ader, BP 40109, 86961 Futuroscope-Chasseneuil Cedex, France. Contact e-mails: luciana-maria.bortoluci-ormastroni@ensma.fr, jonathan.cormier@ensma.fr INMACULADA LOPEZ-GALILEA, BENJAMIN RUTTERT, and SEBASTIAN WEBER are with the Chair of Materials Technology, Institute for Materials, Ruhr-Universität Bochum, Universitätsstr. 150, 44801 Bochum, Germany.

Manuscript submitted August 5, 2022; accepted October 23, 2022.

Article published online November 27, 2022

or expected to be used for future ones. This contribution provides the analysis of these two HIP-heat-treated SX Ni-based superalloys (ERBO/1 and CMSX-4 Plus) under very high cycle fatigue regime and high temperature.

The very high cycle fatigue regime is of particular importance because vibratory fatigue can be considered a severe damaging load, especially in military aero-engines.^[21] Therefore, it leads to a certifying criterion of airfoils according to airworthiness authorities (*e.g.*, EASA and FAA), since the loading due to vibratory stresses turns out to be a safety requirement of aero-engines.^[11,12,23] This study focuses on the very high cycle fatigue improvement of Ni-based SX superalloys subjected to a new type of integrated HIP heat treatment.

II. MATERIAL AND TECHNIQUES

A. Chemical Composition, Heat Treatment Parameters and Microstructure of the Used Alloys

In this work the SX Ni-based superalloys ERBO/1 (CMSX-4 type) and CMSX-4 Plus are investigated, whose chemical compositions are listed in Table I. The used ERBO/1 specimens were machined from plates casted by Doncasters Precision Castings with a thickness of 20 mm, while the CMSX-4 Plus specimens were machined from rods casted by Safran Aircraft Engines with a diameter of 40 mm.

A first batch of ERBO/1 and CMSX-4 Plus was subjected to their standard solution heat treatment according to References 25 and 14, respectively. A second batch of the superalloys was subjected to high-pressure heat treatments (IHT), for the case of ERBO/1 according to Reference 22, while for the case of CMSX-4 Plus, the IHT heat treatment was developed in the present work.

The exact values of the parameters that define the heat treatments applied are listed in Table II for both studied materials. Due to the novelty of applying a high-pressure heat treatment to CMSX-4 Plus superalloy, it is explained in detail. High-pressure heat-treatment (solution annealing under pressure within the HIP unit) for CMSX-4 Plus was conducted in a QIH-9 type laboratory scale HIP unit from the manufacturer Quintus Technologies AB (Västerås, Sweden) providing fast cooling rates through the so-called ultra-rapid quenching (URQ®) technology. In this work, the HIP unit is equipped with a two-zone Mo furnace. This set-up allows operating the facility at a maximum temperature of 1400 °C and a maximum hydrostatic Ar pressure of 207 MPa. The temperature is controlled by 4 type-B workload thermocouples that are placed near the specimens and 2 additional type-B zone thermocouples controlling the heating system. The high-pressure heat-treatments in this work were performed under an Ar pressure of 100 MPa. The corresponding time and pressure profiles during HIP exposure are shown in Figure 1 for the case of CMSX-4 Plus. After a carefully selected heating rate, two extended temperature holding

periods of 12 h at 1345 °C and 4 h at 1350 °C were applied (Figure 1(a)). Fast cooling at the end of the high-pressure heat-treatment was achieved by rapid Ar gas quenching (Figure 1(b)). No discrepancies between the 4 thermocouples (T01, T02, T03 and T04) were observed.

After solution annealing or high-pressure heat treatment, respectively, the specimens were subjected to the same standard precipitation hardening heat treatments under inert Ar atmosphere, according to the parameters listed in Table II.

The effect of IHT heat treatment on the ERBO/1 microstructure and its benefit on creep and LCF has been published in References 26 and 27 respectively, and therefore this work is not emphasized here. However, because the IHT heat treatment is applied for the first time on CMSX-4 Plus, the effect of this heat treatment on the microstructure is briefly explained. The CMSX-4 Plus superalloy contain a high amount of refractory elements that coupled with the casting conditions used to obtain 40 mm diameter bars, result in an extremely segregated microstructure. The as-cast microstructure has about 14.1 pct. area fraction of eutectic regions and 0.1 pct. area fraction of porosity as can be observed in Figures 2(a) and (b) (*e.g.*, large eutectics and pores).

The high temperatures applied during the IHT heat treatment on the CMSX-4 Plus specimens result in a homogenized material with no remaining eutectic regions and no remaining cast porosity. The high cooling rate applied to cool the specimens within the HIPping from results in a very fine γ/γ' microstructure (see Figures 2(c), (d), (g) and (h)). However, 0.28 pct. area fraction of IM regions was measured in CMSX-4 Plus HIP specimens (see Figure 2(d)). These unwanted IM regions are associated with the presence of a new type of porosity that has been quantified to be the 0.006 area pct. area fraction. The γ/γ' microstructures after aging of both superalloys with and without integrated HIP treatment are depicted in Figure 3. These microstructure analyses were carried prior to the VHCF tests. The γ/γ' microstructures presented in the HIPed specimens are finer than those derived from the conventional HT route.^[28] On the other hand, the specimens with the IHT heat treatment show a more homogeneous γ/γ' microstructure than the specimens with the conventional HT, which means that the γ/γ' microstructures observed at the DC and ID differ less in those specimens with high-pressure heat treatment. Table III summarizes the main microstructural characteristics of both alloys, with and without HIP treatment.

B. Thermodynamic Calculations

In this work, the Thermo-Calc software together with the TCNI10 thermodynamic database developed for Ni-based superalloys are used to calculate the equilibrium property diagram as well as the solidification path according to the Scheil's equation. The thermodynamic results obtained are used to discuss and understand the as-cast microstructures, as well as to define the IHT heat treatment parameters for the studied superalloys. The calculations have been carried out considering the

Table I. ERBO/1 and CMSX-4 Plus Nominal Chemical Composition (in Weight Percent)

Alloy	Ni	Cr	Mo	Co	W	Re	Al	Ti	Ta	Hf
ERBO/1 ^[22]	bal	6.1	0.6	9.3	6.3	2.8	5.8	1.0	6.8	0.1
CMSX-4 Plus ^[24]	bal	3.5	0.6	10	6.0	4.8	5.7	0.9	8.0	0.1

Table II. Nomenclature and Parameters for Standard Homogenization, HIP and Aging Treatments Performed for the ERBO/1 and CMSX-4 Plus Ni-Based Superalloys

Nomenclature	Solution Heat Treatment	Aging
ERBO/1 ^[25]	1 h/1290 °C + 6 h/1300 °C (150 °C min ⁻¹) → 800 °C/AQ	4 h/1140 °C/AQ + 16 h/870 °C/AQ
ERBO/1 HIP	QIH-9 HIP 1 h/1290 °C + 6 h/1300 °C, 100 MPa Ar pressure → quenching	
CMSX-4 Plus ^[14]	15 h/1340 °C/AQ	3 h/1163 °C + 4 h/1100 °C + 20 h/870 °C/AQ
CMSX-4 Plus HIP	QIH-9 HIP at 12 h/1345 °C + 3 h/1350 °C, 100 MPa Ar pressure → quenching	

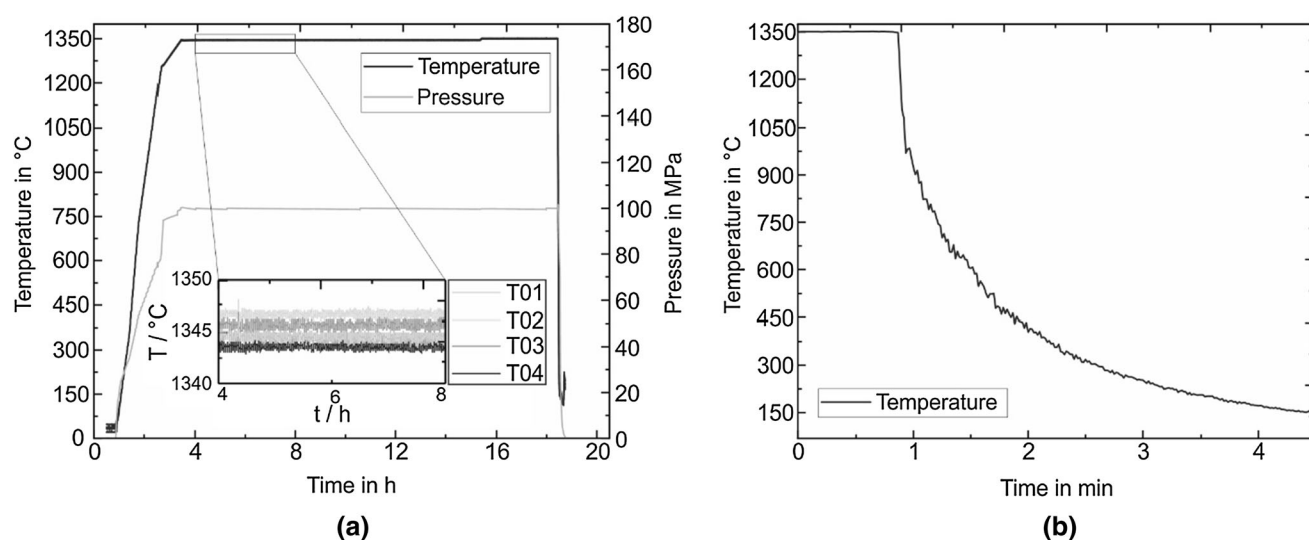


Fig. 1—High-pressure heat-treatment of CMSX-4 plus: Integrated HIP treatment cycle as temperature and pressure over time plot with two holding steps for 12 h at 1345 °C and 3 h at 1350 °C and 100 MPa isostatic pressure (a). Fast HIP cooling that cools within less than 60 s from 1350 °C to a temperature below 750 °C, the small deviation of the recorded temperature signals is because of the thermocouple position which is located on the upper part of the HIP-furnace while the rest is located close to the specimen (b).

composition of the two studied superalloys (Table I). However, since similar results have already been published for the authors by some of ERBO/1 in Reference 29 using the previous thermodynamic database TCNI9, in this work, only the results obtained for CMSX-4 Plus are detailed, referring to those published for ERBO/1 when necessary.

C. Very High Cycle Fatigue Tests

VHCF tests were performed using hourglass-shaped specimens.^[30] Electro-discharge machining and subsequent turning were used to obtain the final shape extracted the specimens. Thirteen specimens for ERBO/1 and five specimens for CMSX-4 Plus were machined in-house. A thickness of 0.2 mm was first removed from

the original diameter by SiC grinding to eliminate the residual stresses inherited from the machining steps. This polishing step is essential to avoid surface recrystallization during high-temperature fatigue tests. Thereafter, the surfaces were ground and polished to a final mirror polish (1 μm diamond suspension) with the final steps parallel to the loading axes.

Strain-controlled VHCF tests were performed at 1000 °C (± 2 °C), $f = 20 \pm 0.5$ kHz, $R_\epsilon = -1$ with an ultrasonic fatigue machine used in previous studies.^[11,14,15,23,30–32] The fatigue tests were performed with a sinusoidal waveform. An induction coil was used as a heating source, the power of which was controlled by a closed-loop with a dual-wavelength pyrometer measuring the specimen's central temperature. Before starting the tests, a pre-heating of 45 minutes at 1000 °C was

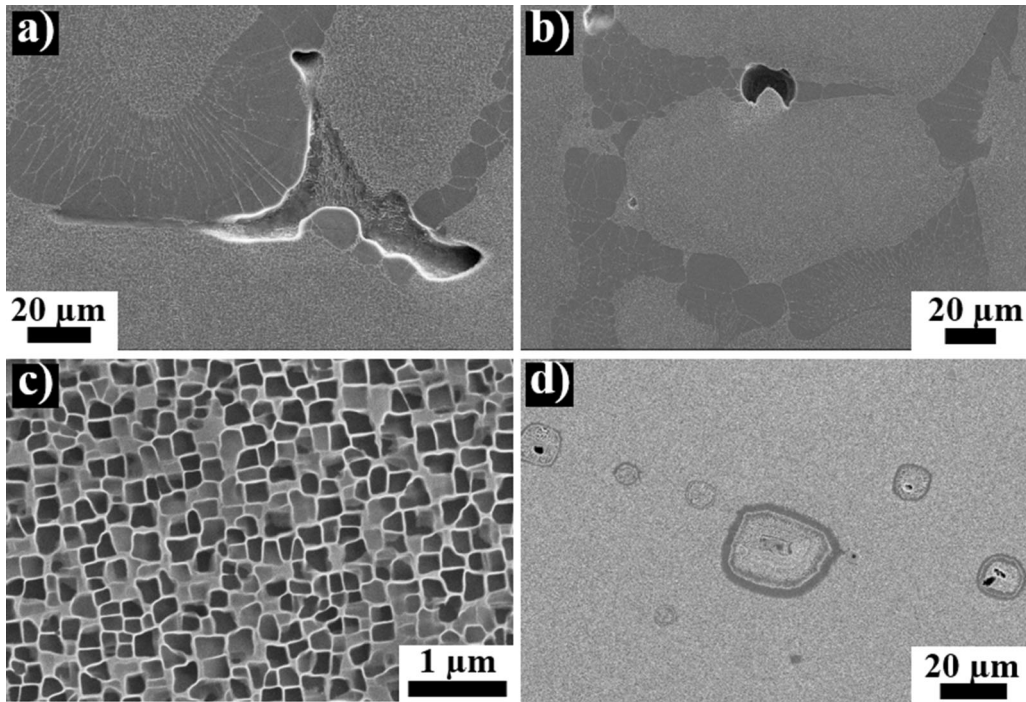


Fig. 2—Microstructure of CMSX-4 Plus before and after IHT. Large pore in as-cast state (a). Representative eutectic region in as-cast state (b). γ/γ' microstructure at the dendrite core in CMSX-4 Plus HIP directly after the IHT (c). Incipient melting in CMSX-4 Plus HIP after IHT (d).

applied to stabilize the surface oxides and resulting surface emissivity.

D. Post-mortem Analyses

Optical and scanning electron microscopy (OM and SEM, respectively) were employed to perform post-mortem observations. Fractographic analyses were carried out using a field emission gun (FEG) scanning electron microscope (SEM) JEOL JSM-7000F operating at 25 kV. In addition, longitudinal sections were mirror polished up to a 1 μm diamond paste finish to observe the microstructure under secondary (SE) and backscattered electrons (BSE) imaging modes on the same equipment operating at a work distance of ≈ 10 mm.

For the electron backscatter diffraction (EBSD) analyses the specimens were polished using colloidal silica solution (particle size 0.04 μm). The analyses were performed to characterize the crystallographic orientation around the internal crack initiation. It was performed using a second JEOL JSM-6100 SEM, operating at 25 kV, and the orientation imaging microscopy (OIM) software EDAX, version 6.1. A scanning step size of 0.2 μm was chosen.

III. RESULTS

A. Development of the Integrated HIP Treatment for CMSX-4 Plus Alloy

A detailed characterization of the as-cast microstructure is essential to define the conditions for the necessary subsequent heat treatments. The microstructure of

CMSX-4 Plus in as-cast condition has been presented in Sect. 2.1. On the other hand, performing specific thermodynamic calculations allows knowing the transformation temperatures of the main phases present in the studied material, and this information is essential for a safe and reliable design of heat treatments.

The use of the Scheil's equation allows accessing the redistribution of the solute during solidification assuming that there is a perfect mixture in the liquid phase and there is no diffusion in the solid phase. The results derived from the Scheil calculation for the CMSX-4 Plus superalloy are shown in Figure 4(a), where the fraction of phases is represented as a function of temperature. The transformation temperatures of the phases considered in the Scheil's calculation are listed in Table IV.

According to the Scheil calculations, the solidification starts at 1408 $^{\circ}\text{C}$ and ends at 1168 $^{\circ}\text{C}$. The solidification begins with the nucleation and growth of the γ phase (matrix) and at 1337 $^{\circ}\text{C}$ the γ' phase nucleates, reaching a phase fraction of about 11.4 pct at the end of solidification. As the temperature decreases and approaches the end of solidification, the sigma (σ) and H_L12 phases precipitate, reaching a maximum individual phase fraction of 0.05 and 0.12 pct, respectively. During the Scheil solidification, the nucleation of the primary γ' -phase takes place at a temperature of 1337 $^{\circ}\text{C}$ when the amount of liquid is 25.4 pct. The predicted amount of primary γ' , 11.4 pct is in good relatively agreement with the eutectics area fraction measured in the CMSX-4 Plus as-cast microstructure, 14.1 area fraction.

Figure 4(b) shows the property diagram, molar fraction of the phases vs temperature, calculated under equilibrium conditions for the CMSX-4 Plus superalloy.

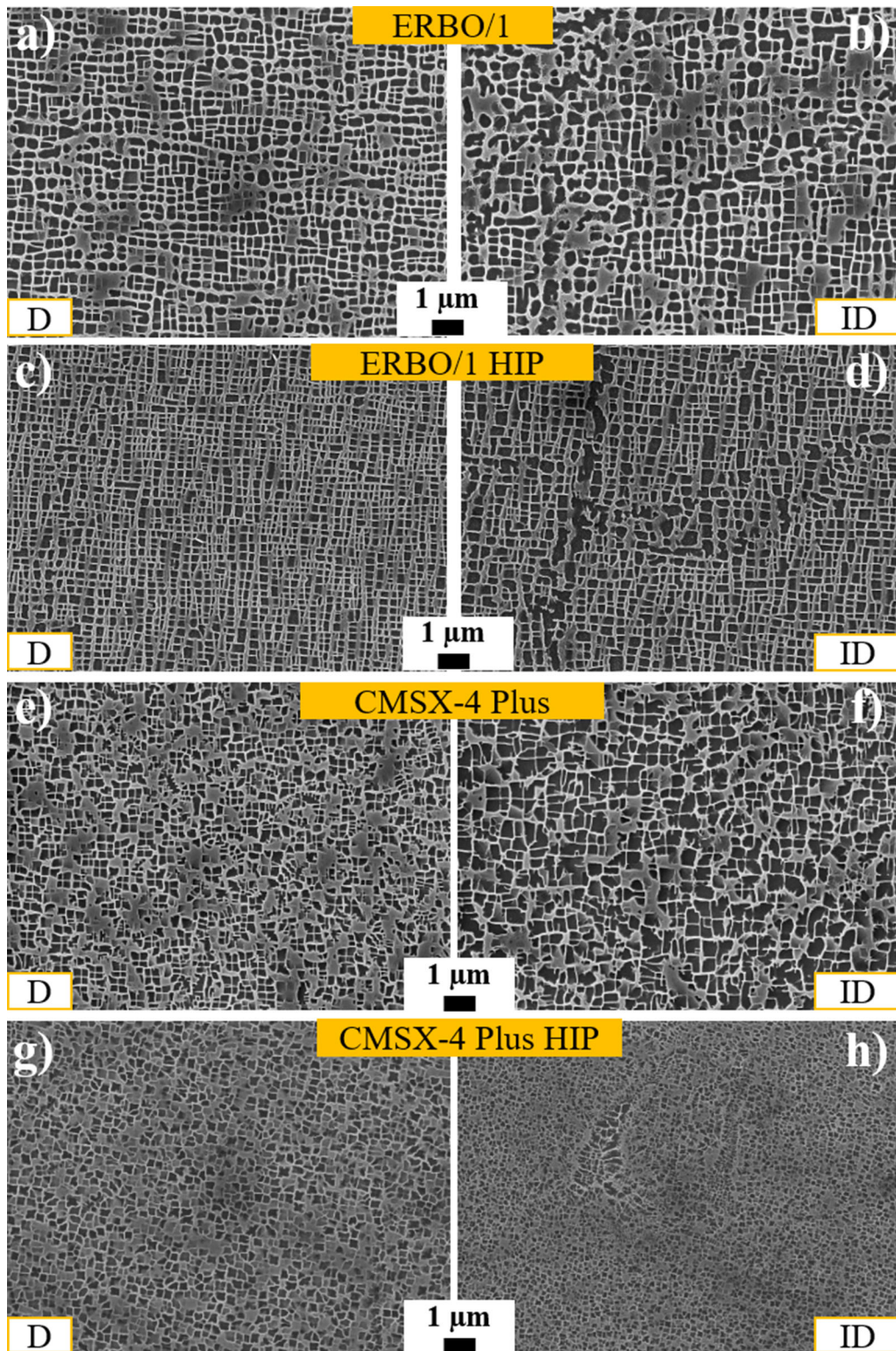


Fig. 3— γ/γ' microstructure at dendrite cores (D) and at interdendrite zones (ID) of ERBO/1 ((a) and (b) resp.), ERBO/1 HIP ((c) and (d) resp.), CMSX-4 Plus ((e) and (f) resp.), and CMSX-4 Plus HIP ((g) and (h) resp.) after the corresponding aging heat treatments. Observations performed in along $a \approx (001)$ plane.

This Figure shows that solidification begins at 1408 °C (liquidus temperature) with the γ phase and that solidification ends at 1352 °C (solidus temperature). At 1302 °C, the γ' phase appears through a solid–solid

transformation, reaching a phase fraction of about 72 pct at 800 °C. At temperatures below 1079 °C, the presence of σ phase is calculated, the maximum amount

of which does not reach values higher than 1.8 pct mole fraction at 800 °C.

Considering the as-cast microstructure, as well as the results of both types of thermodynamic calculations, the integrated HIP heat treatment was designed with two main holding steps: the first at 1345 °C for 12 h and the second at 1350 °C for 3 h. The first step conducted at $T > T_{\gamma' \text{ solvus}}$ aimed to dissolve the γ' -phase while the second one carried out at $T < T_{\text{solidus}}$ aimed to further accelerate the homogenization procedures without achieving the melting of the material. In addition, a pressure of 100 MPa was applied during the heat treatment to close the casting porosity and the quenching option was selected to cool the specimens to develop a uniformly distributed and fine γ/γ' microstructure. It is recalled here that Figure 1 shows the temperature—time profiles of the IHT performed with the CMSX-4 Plus specimens. Figure 2(c) shows the fine γ/γ' microstructure derived from the application of the quenching option. During this lengthy high pressure solution annealing heat treatment, the reduction of the segregation resulting from the casting process is expected, as well as the dissolution of all the distinct phases in the γ -matrix. If a high degree of chemical homogenization of the material is achieved, no IM regions should be observed after the IHT heat treatment. However, as shown in Figure 2(d), the presence of IM regions occurs, and this was quantified in an amount of 0.28 pct in area fraction.

After the IHT heat treatment, the specimens were subjected to a three-step aging heat treatment. The third aging step of 20 h at a temperature of 870 °C aims to reach the ≈ 70 vol pct of γ' phase predicted by the equilibrium thermodynamic calculation. The γ/γ' microstructures obtained after aging are shown in Figures 3(g) and (h).

B. VHCF Performance and Fractography Analyses

The alternating stress (σ_a) as a function of the number of cycles to failure (Nf) diagram gathering all the VHCF results obtained in this study is presented in Figure 5. The fatigue life improved by two decades for ERBO/1 superalloy and by three decades for CMSX-4 Plus in the [140–240 MPa] alternating stress range by performing a high-pressure heat-treatment.

After mechanical testing, fractographic observations were performed. The fracture analysis of ERBO/1 specimens was already presented in detail by Bortoluci *et al.*^[33] Crack initiation from internal solidification pores was systematically obtained, these critical pores having a maximum diameter ranging from 80 to 200 μm (Figures 6(a) and (b)). The CMSX-4 Plus specimens consistently presented crack initiation from solidification pores ranging in size from 100 to 230 μm (Figures 6(c) and (d)). Such a crack initiation mode has already been well detailed in the literature.^[12,13,30]

The quite pronounced scatter in VHCF life of non-HIPed ERBO/1 and CMSX-4 Plus specimens displayed in Figure 5 results from the variation in casting pore size serving as the main crack initiation site (Figure 6) since specimens were machined out from a

thick SX plate and 40 mm diameter rods. In fact, using the same casting parameters, large SX castings are known to introduce larger solidification pores, overall reducing the fatigue life.^[9,12,34] Therefore, the non-HIPed specimens will not be further analyzed. Only the general trend of the values obtained is used to evaluate the behavior of the specimens with an IHT heat treatment, *i.e.* HIPed ones.

Fractographic observations of the HIPed specimens uncovered a rather unusual crack initiation zone after the VHCF tests. Figure 7 depicts two examples of them. The samples failed at zones with distinct characteristics (i) from a significant feature with no rough zone (Figures 7(a) and (b)) or (ii) from a feature surrounded by the rough zone (Figures 7(c) and (d)). ERBO/1 specimens presented both characteristics, while CMSX-4 Plus presented just the (ii) characteristic. However, it was not possible to identify the specific crack initiation site from the fractography observations.

C. Microstructure Analysis Along the Longitudinal Section

Figure 8 shows a longitudinal section intercepting the crack initiation site of the ERBO/1 HIP sample shown in Figure 7(a). The crack initiation site is indicated by the red dotted square in Figure 8(a). Indeed, Figure 8(b) and (c) show what seems to be a remaining pore at the top of the fracture surface, indicated by the blue arrows. Figures 8(d) through (f) also show a non-planar crack propagation. Such a crack propagation path is not expected for Ni-based SX superalloys failing in VHCF, which usually show a crystallographic crack path out of the rough zone.^[10–16,23,35] The γ/γ' microstructure around the HIPed casting pores is heterogeneous (see green dotted lines in Figure 8(d)).

Figure 9 shows the longitudinal analysis of the CMSX-4 Plus HIP sample (Figure 7(c)). It was not possible to reach the crack initiation site in the observation plane. On the other hand, Figure 9 shows the presence of incipient melting (IM), which is surrounded by an orange dotted line in Figure 9(a). The IM structures in the CMSX-4 Plus microstructure were observed after the IHT heat treatment before the VHCF tests (Figure 2(d)). The size of the IM regions after HIP was measured to be in the 10–30 μm range and did not change during VHCF testing. The IM are filled with intermetallic phases and what is believed to be freshly formed pores of very small size.

D. EBSD Microstructure Characterization of HIPed Samples

The SEI and BSE images do not provide much information on crack initiation sites. Figure 10(a) is a longitudinal section EBSD microstructure characterization of the ERBO/1 HIPed sample shown in Figures 7(a) and (b). The image quality (IQ) is superimposed onto the inverse pole figure (IPF) close to the fracture surface in Figure 10(a). The failure is recognized to be along a (111) plane (see Figure 10(a)), a typical crack propagation for Ni-based SX superalloys.

Table III. Metallurgical Characteristics of the ERBO/1 and CMSX-4 Plus With and Without Integrated HIP Treatment in the As-Aged Condition

Nomenclature	ERBO/1 ^[25]	ERBO/1 HIP	CMSX-4 Plus ^[14]	CMSX-4 Plus HIP
Eutectics' Area Fraction (Pct)	0.16	0.25	0	0
Incipient Melting' Area Fraction (Pct)	0	0	0	0.28
Pores' Area Fraction (Pct)	0.388	0.018	1	0.006
γ' Size—Dendrite Core (nm)	480 \pm 15	400 \pm 95	525 \pm 91	570 \pm 92
γ Channel Width (nm)	50 \pm 7	60 \pm 7	60 \pm 13	60 \pm 17
γ/γ' Volume Fraction (Pct)	65	60	60	58

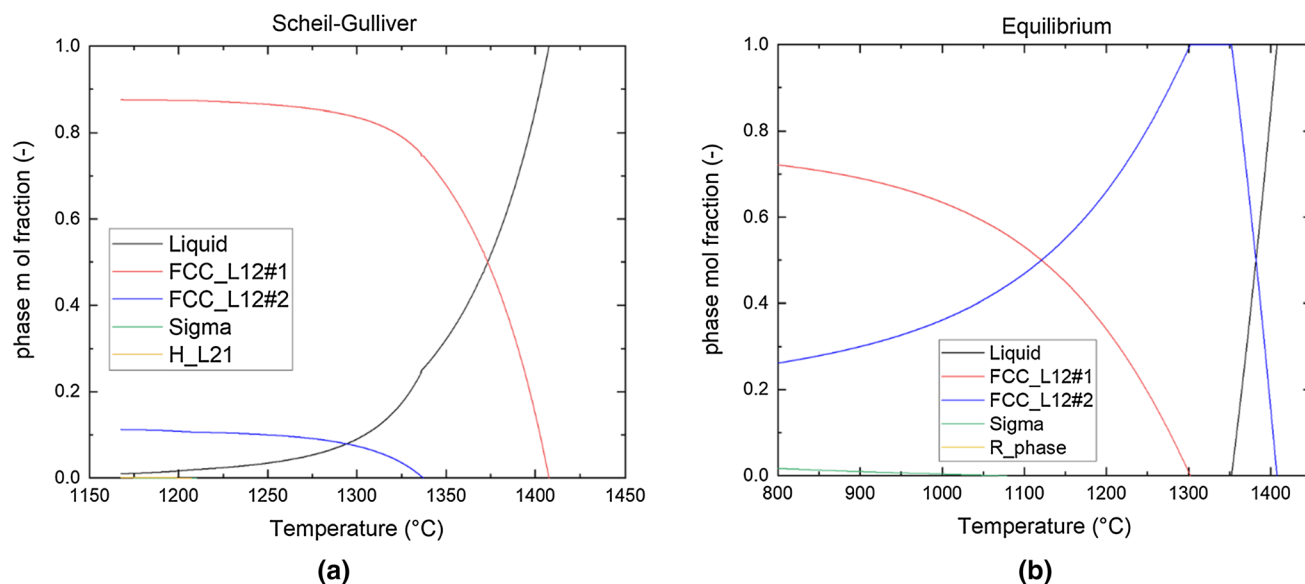


Fig. 4—Thermodynamic calculations for the nominal composition of CMSX-4 Plus using TCNI10 database: Scheil solidification diagram, phase molar fraction vs temperature (a). Property diagram, phase molar fraction vs temperature, under equilibrium conditions (b).

Table IV. Main Phase Transformation Temperatures According to Scheil's and Equilibrium Calculations for the CMSX-4 Plus Superalloy

	Liquidus	Solidus	γ' solvus	σ Solvus	H_L12 Solvus
Scheil	1408	1168*	1337	1210	1207
Equilibrium	1408	1352	1302	1079	—

Temperature values in °C. (* Solidus temperature is calculated in the presence of liquid in an amount less than 0.01 pct)

The IQ and IPF maps indicate a crystallographic orientation gradient within the SX bulk. Figures 10(c) and (d) indicate the presence of what seems to be a remaining casting pore. Figure 10(e) up to h shows the analyses of the particular region adopting different filters. Many others similar structures (larger and smaller) were observed all over the ERBO/1 HIP sample's microstructure. These features were not identified in the non-HIPed specimens after VHCF tests.

The previous EBSD characterizations of an IM^[14] have shown that the IM, once resolidified in the absence of pressure, exhibits no misorientation compared to the parent material. No characterization of IM after the HIP treatment was found in the literature. The EBSD characterization of the incipient melting developed during the hot isostatic pressure process is presented in

Figure 11. The EBSD map with IQ superimposed to the IPF relative to the loading direction of an incipient melting shows that after the “resolidification” this melted zone exhibits the same crystallographic orientation as the parent SX material. Only very small misorientation of up to 3–4 deg were observed by EBSD, *i.e.* formation of Low Angle Grain Boundaries as in Figure 10(h). A second IM was characterized with the same conclusion (results not shown in this paper). The EBSD characterization shows that the intermetallic phases identified in Figure 9 are TCP phases that precipitates inside the compacted pores surrounded by the IM (see Figure 11(b)). Prior characterizations from the authors have shown that these white particles are very rich in Re, with a local Re content of up to 30 wt. pct. in CMSX-4 Plus.^[14]

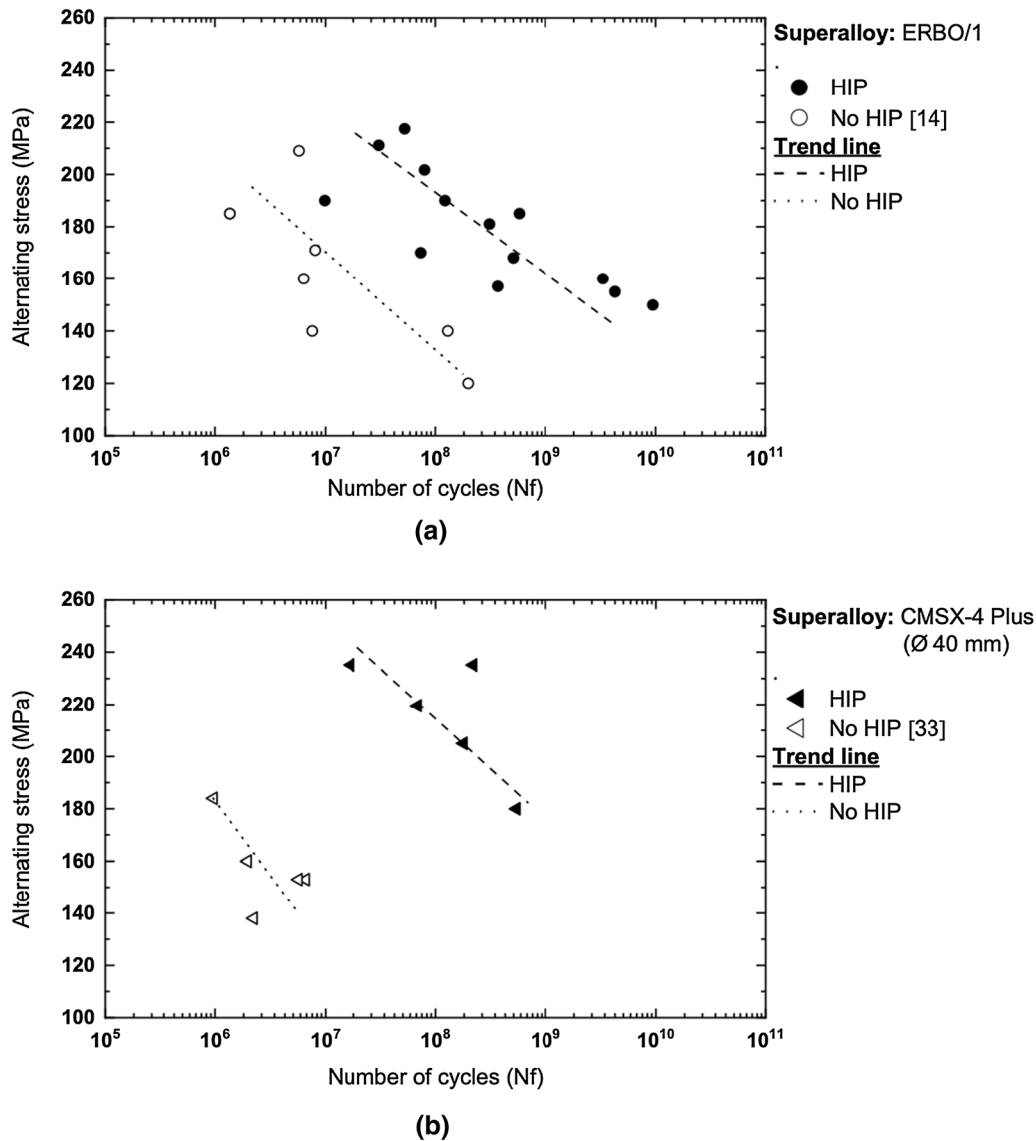


Fig. 5—Individual S-N diagram at 1000 °C, $R_e = -1$, $f = 20$ kHz for ERBO/1 (a), and CMSX-4 Plus (b) with and without HIP treatment results. The alternating stress is plotted as a function of the number of cycles to failure. The non HIPed data are extracted from the literature^[14,33].

IV. DISCUSSION

The HIP treatment performed between γ' -solvus temperatures, and the incipient melting temperature seems to provide the best subsequent VHCF durability. Furthermore, as pore closure during HIPing occurs by plastic deformation, nucleation of low angle grain boundaries/sub-grains in the vicinity of former casting pores were observed both investigated superalloys. Further, even though the superalloy is prone to develop incipient melting like structures, it was shown that these features are not a source of recrystallization. The next topics will discuss the crack initiation site of the HIPed samples, as it was not completely clear after the fracture and the microstructure longitudinal characterization.

A. Integrated HIP Treatment Development and Mechanical Benefits

The results obtained in the study of Kim *et al.*^[36] show that if the HIP process is properly performed it can be an effective substitute for the heat treatment applied for nickel-based superalloys. Even though the conventional HIP process alone is effective for the homogenization annealing, the slow cooling rates provided by conventional industrial HIP-units leads to an irregular γ/γ' microstructure,^[37,38] as a consequence, subsequent heat treatments are necessary to obtain the ideal nickel-based superalloy microstructure known to maximize creep strength.^[6] The integrated HIP treatment is a proposal to merge the standard solution annealing heat treatment and the HIP heat treatment into one processing step

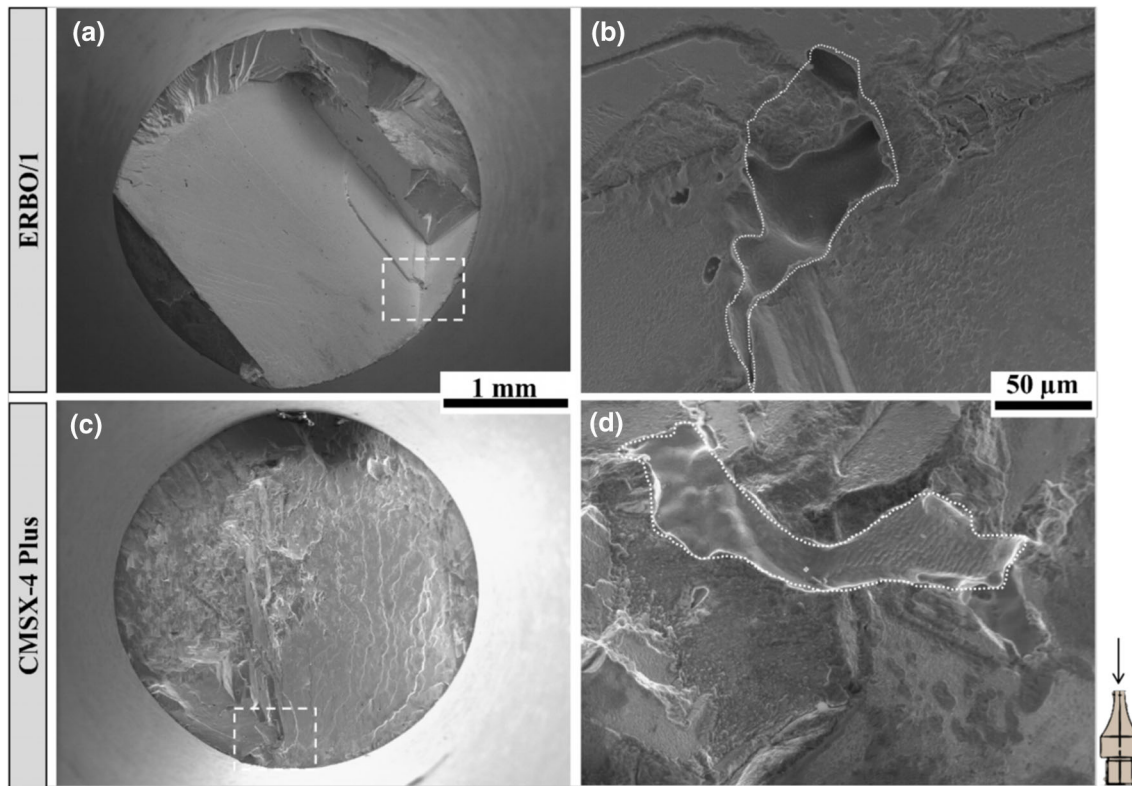


Fig. 6—Fractographic observations of non-HIPed specimens with main crack initiation from solidification pores. ERBO/1 ($\sigma_a = 160$ MPa, with $N_f = 6.6 \times 10^6$ cycles) (a) and magnification of crack initiation zone (b). Detail of the presence of a casting pore with a diameter of $\approx 170 \mu\text{m}$. CMSX-4 Plus ($\sigma_a = 160$ MPa, with $N_f = 1.9 \times 10^6$ cycles) (c) and magnification of crack initiation zone (d). Detail of the presence of a casting pore with a diameter of $\approx 170 \mu\text{m}$. The dotted white lines indicate the critical casting pore.

because fast cooling rates can be provided. From the HIP parameters (pressure, temperature, holding time and cooling speed) the main effect on the porosity and the γ/γ' microstructure is the temperature and cooling rate control respectively. HIP temperatures above the γ' solvus temperature allow the fastest and most effective reduction of the porosity, because only the soft γ phase is present.^[39] The recent possibility of cooling the samples from the maximum HIP temperature with a fast cooling, faster than 200 K/min, results in a fine and homogeneous distribution of γ' particles, which requires no additional re-resolution annealing treatment to again dissolve the developed γ' particles during the extremely short cooling time.^[40]

However, there are difficulties to design and control such integrated HIP treatment and these difficulties are amplified due to the superalloy's chemistry. The heat treatments required to homogenize the single crystals superalloys have a tight control of the temperature/time to avoid incipient melting.^[41] Thus, designing an integrated HT that allow obtaining a good homogenization of the material in an adequate time requires a compromise of temperature and time. One of the supports to the development and application of HT is the CALPHAD technique that couples the phase diagrams and the thermomechanical properties of the respective alloy system.^[42] The use of these thermodynamic databases in order to design heat treatments is useful as a first guidance, despite the large number of interpolations that

this software performs from binary and ternary phase diagrams.

Most of the HIP treatments are applied after the solution heat treatment, but to diminish the impact of HIP treatment costs, the heat treatment of this study was integrated to the HIP treatment. A second choice was to increase in the maximum temperatures in the integrated heat treatment for the CMSX-4 Plus superalloy with respect to those used in the conventional heat treatment. It resulted in a good homogenization of the material (more effective elimination of segregation), leading to an improvement of final mechanical properties (Figure 5). These choices have introduced metallurgical defects into the superalloy microstructure, which may have prevented for an even better performance in the tests. By means of plastic deformation, the integrated HIP treatment within the γ' super solvus temperature controlled the pore shrinkage, leading to the healing surfaces (Figures 8 and 10) in good agreement with.^[39] These features were as well observed by Zheng *et al.*^[43]

Note that the cooling rate after HIP solution treatment mostly controls creep/tensile properties, see, *e.g.* Reference 44. The integrated HIP treatment removed most of the solidification pores, increasing in at least two decades the VHCF life of the ERBO/1 and CMSX-4 Plus samples, being beneficial from a mechanical properties point of view. It is known that the HIP treatment exerts a stronger influence on HCF than on LCF^[20] and

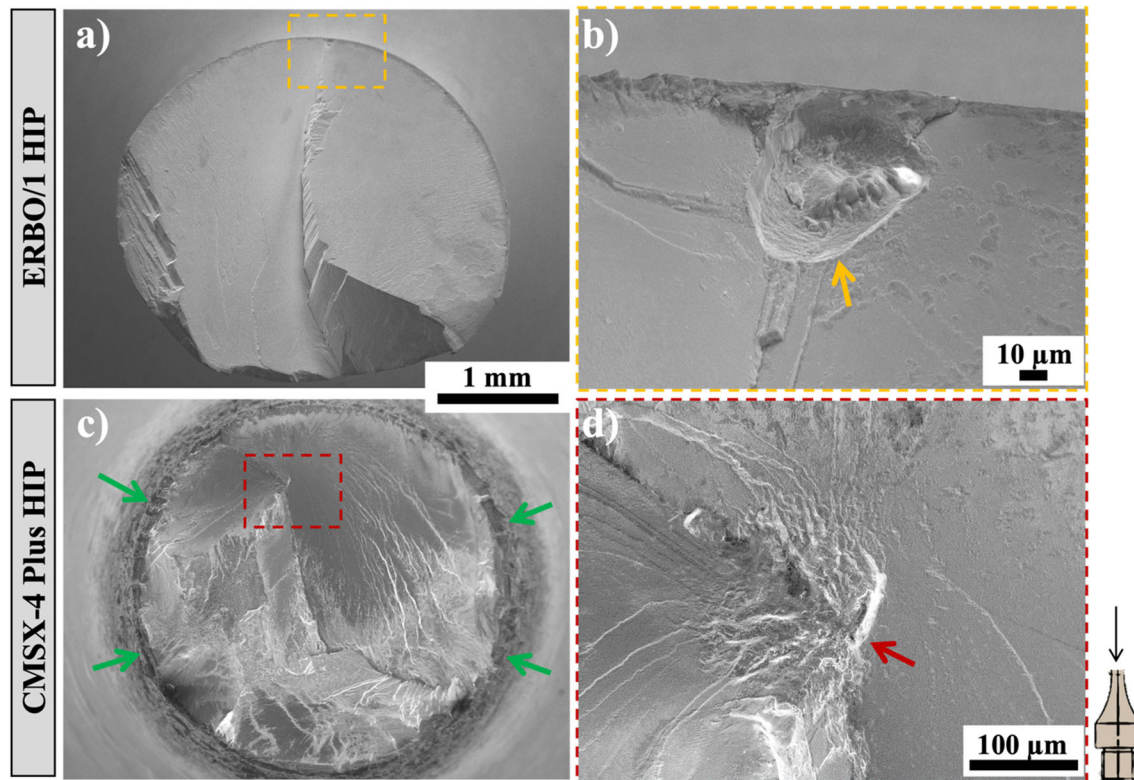


Fig. 7—Fractographic observations of HIPed specimens. ERBO/1 ($\sigma_a = 190$ MPa, with $N_f = 9.8 \times 10^6$ cycles) (a), CMSX-4 Plus ($\sigma_a = 180$ MPa, with $N_f = 5.4 \times 10^8$ cycles) (c) and magnification of crack initiation zone ((b) and (d) respectively). The arrows indicate the main crack initiation site. The green arrows indicate the high oxidation activity in the CMSX-4 Plus specimens (Color figure online).

seems to have an even stronger effect for the VHCF life of Ni-based SX superalloys at high temperature test regimes.

B. On the Impact of Compacted Pores and Casting Pores on Fatigue Life

The HIP treatment is usually employed to suppress or decrease the effect of critical casting pores on the fatigue life. At elevated temperatures (1000 °C) and ultrasonic fatigue conditions (20 kHz, and $R_e = -1$) the casting pores are known to control the crack initiation process.^[11,12,14,16,30,35,45–47] Then, solidification methods and heat treatments were modified to control casting pore size and distribution. Consequently, it increased the superalloy performance under extreme environments. Classically, increasing the solidification rate using the LMC method or processing the superalloy by HIP treatment leads to the improvement of the superalloy fatigue performances.^[9,12,48] However, according to the literature, there is no full understanding of the influence of this treatment on the VHCF crack initiation mechanism(s).

According to the fracture surface and longitudinal observations, the pore closure mechanism of ERBO/1 samples occurred by viscoplastic deformation forming such a feature as the one observed in Figure 10 with a nearly 100 μm in size. In addition, specimens were HIPed at super-solvus temperature, increasing the

plastic flow rate under these extreme temperatures. The orientation deviation around the features depicted in this sub-section is also similar to the plastic strain distribution calculated by finite elements in the literature.^[20,39,49] Indeed, Epishin *et al.* show that the von Mises stresses are highly heterogenous at the pore surface during the compression, leading to significant and very localized plastic strains.^[20] Even though it is not possible to quantify plastic strain within individual grains using EBSD derived misorientation values, the relationship between misorientation and plastic strain is affected by the heterogeneity in slip (discontinuous) and lattice rotation (continuous) activity.^[50]

In short, after the HIP treatment, the compacted casting pore morphology was defined as a sub-grain structure with LAGB (see, *e.g.*, Figures 10 and 11). The sub-grain structure in Figure 10 has $a \approx 100 \mu\text{m}$ diameter; structures with size up to $\approx 5 \mu\text{m}$ diameter were observed in the ERBO/1 HIP sample microstructure. Thus, the diameter of the sub-grains structures is as scattered as the casting pores in the non-HIPed specimens. The authors believe that the compacted features are directly proportional to the pre-existing casting pore size. However, the HIP treatment still improved the lifetime of ERBO/1 by two decades, even when the sub-grains structures have diameters as high as 100 μm . Therefore, just comparing the VHCF life analysis, such a feature appears to be less damaging than the casting pores onto the VHCF life.

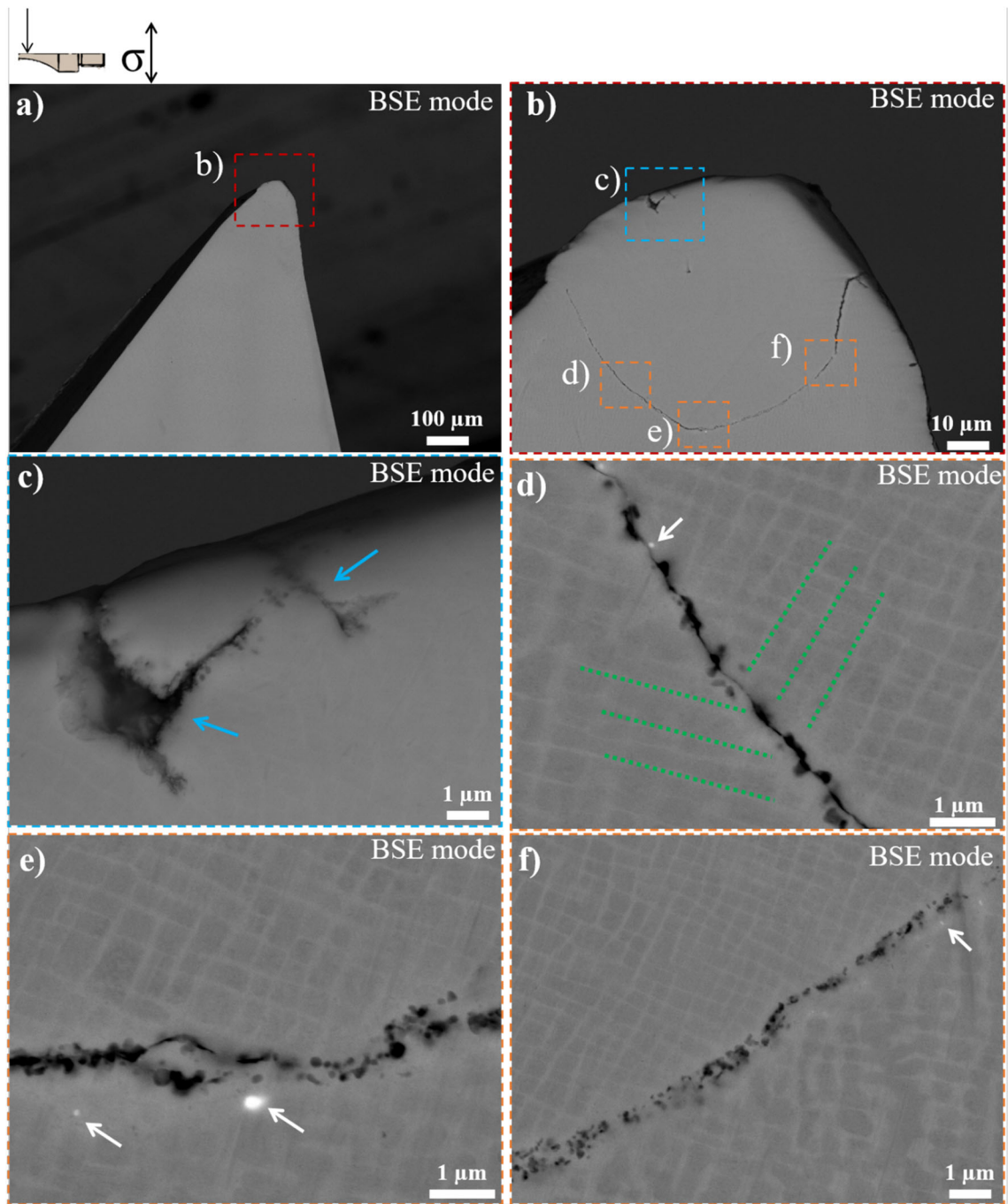


Fig. 8—Longitudinal section of Fig. 7(a), ERBO/1 HIP sample ($\sigma_a = 190$ MPa, with $N_f = 9.8 \times 10^6$ cycles). Analysis of the crack initiation zone (a), magnification of top zone indicated by the red square (b). Magnification of the remaining pore indicated by the blue square in (b) and the blue arrows (c), magnification of the crack zone around the HIPed casting pore (d), (e), and (f). These SEM observations were done using a BSE observation mode. The white arrows indicate the TCP phases appearing in bright elementary contrast. The green dotted lines in (d) indicate the γ channels direction. A HIPed casting pore is presented in (b) and magnified in (c) (Color figure online).

Furthermore, the crack initiation and propagation mechanism seem to be similar between the samples HIPed and the non-HIPed vacuum furnace treated samples. For example, in Figures 8(d), (e) and (f) were identified the presence of cavities and TCP precipitates at the interfaces of the sub-grains structure and the superalloy bulk. These zones are very similar to the

rough zone characteristics uncovered by Cervellon *et al.*^[13]

Based in Figure 10, one of the key questions is how the local misorientation introduced in the vicinity of closing pores during the HIP process may affect the VHCF life. In fact, it is known from Cervellon *et al.*^[12] that the presence of LAGB in DS Ni-based superalloys does not significantly affect the VHCF life at 1000 °C/

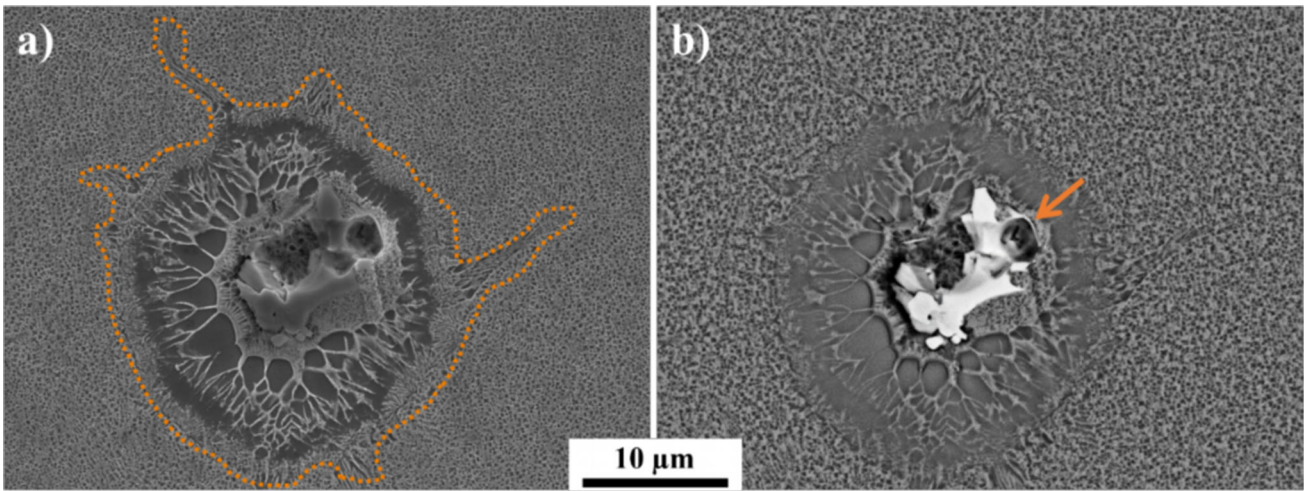


Fig. 9—Longitudinal section analysis of Fig. 7c CMSX-4 Plus HIP sample ($\sigma_a = 180$ MPa, with $N_f = 5.4 \times 10^8$ cycles). Incipient melting indicated by the orange dotted line observed in SEI (a) and BSE (b) mode (Color figure online).

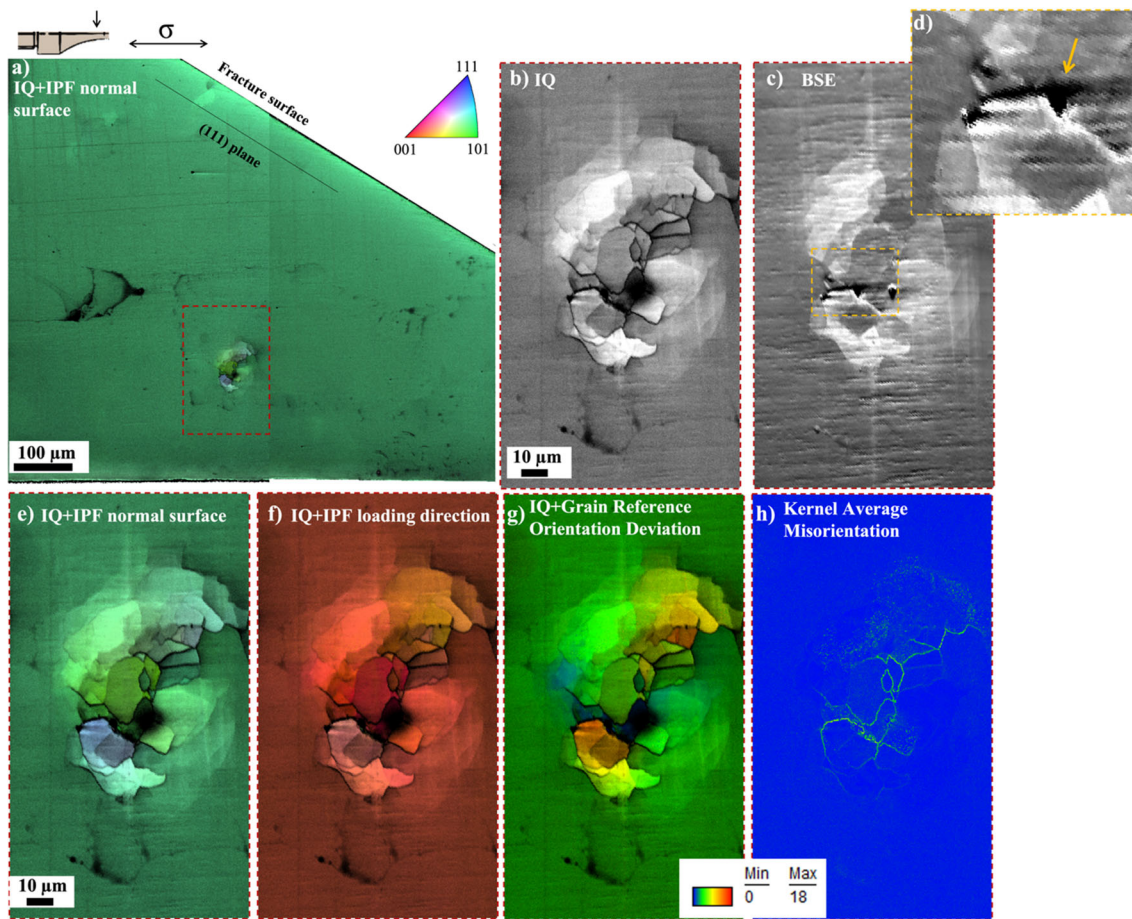


Fig. 10—EBSD characterization of ERBO/1 HIPed sample illustrated in Fig. 7(a) ($\sigma_a = 190$ MPa, with $N_f = 9.8 \times 10^6$ cycles) focusing on an almost fully closed pore. The analysis was carried close to the fracture surface. Sample's image quality (IQ) + inverse pole figure (IPF) (a). Magnification of the feature indicated by the red dotted rectangle, IQ (b), BSE (c), magnification of the yellow dotted square presenting a remaining casting pore (yellow arrow) (d), IQ + IPF normal to the surface (e), IQ + IPF relative to loading direction (f), IQ + grain reference orientation deviation (g), and Kernel average misorientation (h).

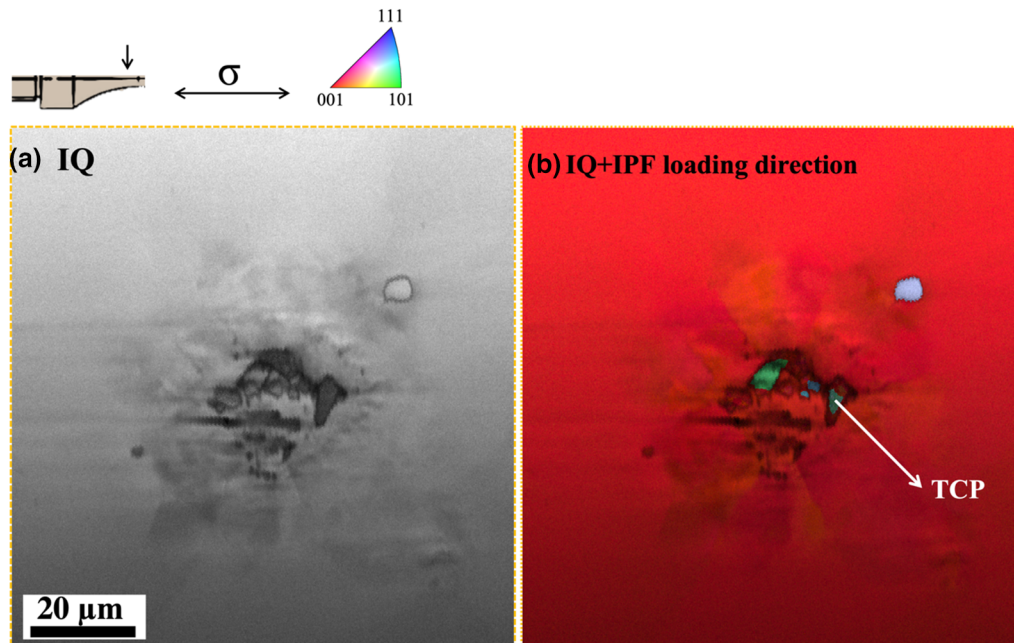


Fig. 11—EBSD characterization of CMSX-4 Plus HIPed sample ($\sigma_a = 180$ MPa, with $N_f = 5.4 \times 10^8$ cycles) illustrated in Fig. 7(c). The characterization focusses on an incipient melting. Sample's image quality (IQ) (a) and IQ superimposed to the IPF normal to the relative loading direction (b). The white arrow indicates the TCP phases.

$R_e = -1$ compared to the pure single-crystalline same alloy (with the same solidification parameters).

Although HIP treatment is associated with increased costs, which has to be proven in the future, the benefits obtained from its use (improvement of fatigue life) is greater than the associated additional cost. It is worth noting that scatter is also reduced which in terms can be related to a more robust HIPing methodologies and safer operation of the HIP treated components. Also, the HIP treatment is a powerful tool to recover the γ' rafting after the creep tests or coarsened microstructures in general.^[51] The HIP treatment suppress the diffusion of the alloying elements during phase change, resulting in a refined and homogenized microstructure.^[52] Also, the restoration of microstructural and material properties under HIP treatment of creep specimens showed to be effective to the cavity healing. The appropriate HIP schedule followed by the heat treatment process seems to improve the rupture life of damaged alloys.^[53] The risk of recrystallization has, however, to be evaluated from a component point of view.

C. Incipient Melting After HIP Treatment and Its Influence on the Crack Initiation

From the previous study,^[14] introducing nearly 20 pct of IM in CMX-4 Plus Bridgman rods did not influence the LCF, HCF, VHCF fatigue life or the high temperature tensile and creep properties of CMSX-4 Plus superalloy. Moreover, the specimens with and without the IM presented the fatal crack initiation at casting pores with comparable diameter size. Furthermore, no crack initiation was identified at IM by Bortolucci *et al.*^[14] in CMSX-4 Plus non-HIPed samples.

It has already been shown that such IM areas may develop even for HT at close-solvus conditions^[54] it was hence not surprising to see IM in the present case as HIP was performed at nearly solidus conditions. One has to note that under isostatic pressure, both the γ' solvus and the IM temperature slightly rise.^[14,55]

The VHCF tests performed on the CMSX-4 Plus HIPed samples with ≈ 0.3 pct of IM allowed to understand the role played by the IM developed during the integrated HIP treatment. First, the IM development at high temperature and high isostatic pressure of 100 MPa led to structures with almost the same crystallographic orientation as the parent SX material. It implicates that such structures are not source of recrystallization with high angle grain boundaries whatever the heat treatments conditions.

Even though the HIP treatment led to the (quasi-) complete annihilation of pores, the fracture analysis has shown that the CMSX-4 Plus samples still failed at internal critical microstructural features. One may speculate that the IM influenced the crack initiation may be one of these critical features. However, the authors identified no evidence of crack initiation at these features. Moreover, the CMSX-4 Plus superalloy is Re-rich and, thus, prone to precipitate TCP phases.^[56,57] After the VHCF, tests the IM regions are filled with TCP phases as shown in Figures 9 and 11. Despite these TCP phases are known to be brittle at low temperatures and to lead to interfacial decohesion in LCF conditions at a high temperatures of 950 °C^[58] and in VHCF^[30] at 1000 °C, no specific impact has been observed here in CMSX-4 Plus. This may be a result of their small size and low area fraction compared to the other defects such as the remaining casting pores (compacted/

homogenization) of ≈ 1 to $5 \mu\text{m}$ diameter observed in the CMSX-4 Plus microstructure (see Figure 2(d) and Table III).

The authors propose that the improvement of the IHT by decreasing the temperature of few degrees would avoid the formation of such IM islands. Even though the authors believe that the IM islands do not influence the crack initiation, it would be essential to analyze the VHCF crack initiation of CMSX-4 Plus HIPed samples without such structures to explore this subject.

V. CONCLUSIONS

The very high cycle fatigue life of ERBO/1 and CMSX-4 Plus Ni-based superalloys subjected to an integrated HIP heat treatment was investigated in this study. The tests were performed at 20 kHz, 1000 °C and $R_e = -1$. From the present study, the following main conclusions were drawn:

- An integrated HIP heat treatment with ultra-rapid cooling has been developed and applied for the first time to CMSX-4 Plus superalloy.
- The integrated HIPing process increases the fatigue life of the two Ni-based SX superalloys studied in this work, ERBO/1 and CMSX-4 Plus, by at least two decades when performed accurately.
- For the first time in the literature, it is shown the sub-grain structures morphology around a compacted casting pore can be a consequence of the HIP treatment. The development of sub-grains boundaries structures has been shown to be less detrimental to the fatigue life than the casting pores.
- Even though a low amount of incipient melting regions develops under high pressure (100 MPa), the melted areas have been shown to resolidify with the same crystallographic orientation as the parent material.

ACKNOWLEDGMENTS

The authors wish to thank Florence Hamon and Jacques Lefort (Physics and Mechanics of Materials Department, Institut Pprime, France) for their help and advice during mechanical testing and microstructural observations. Institut Pprime gratefully acknowledges “Contrat de Plan Etat—Région Nouvelle-Aquitaine (CPER)” as well as the “Fonds Européen de Développement Régional (FEDER)” for their financial support to the reported work. Part of this study was supported by the Nouvelle-Aquitaine French region through the ECOREVE project (project number 2018-1R10122). This study is also part of the “Self-Heating” ANR-Safran-Naval group research chair (Grant # ANR-20-CHIN-0002) involving the Safran Companies, Naval group, ENSTA Bretagne (IRDL) and Institut Pprime. The authors acknowledge funding by the Deutsche Forschungsgemeinschaft

(DFG) in the framework of the collaborative research center SFB/TR 103 through project and T4 (ILG, BR, SW).

CONFLICT OF INTEREST

On behalf of all authors, the corresponding author states that there is no conflict of interest.

REFERENCES

1. M. McLean, G.A. Webster, F.R.N. Nabarro, and A. Cottrell: *Philos. Trans. R. Soc. A*, 1995, vol. 351, pp. 419–33.
2. R.C. Reed: *The Superalloys - Fundamentals and Applications*, Cambridge University Press, Cambridge, First edit., 2006.
3. T.M. Pollock and S. Tin: *J. Propuls. Power*, 2008, vol. 22, pp. 361–74.
4. P. Caron and T. Khan: *Aerosp. Sci. Technol.*, 1999, vol. 3, pp. 513–23.
5. M. Perrut, P. Caron, M. Thomas, and A. Couret: *Comptes Rendus Phys.*, 2018, vol. 19, pp. 657–71.
6. J. Cormier and C.-A. Gandin: in *Nickel Base Single Crystals Across Length Scales*, G. Cailletaud, J. Cormier, G. Eggeler, V. Maurel, and L. Naze, eds., First., Elsevier, 2022, pp. 193–258.
7. S.R. Hegde, R.M. Kearsey, and J.C. Beddoes: *Miner. Met. Mater. Soc.*, 2008, pp. 301–10.
8. S.A. Sajjadi, S.M. Zebarjad, R.I.L. Guthrie, and M. Isac: *J. Mater. Process. Technol.*, 2006, vol. 175, pp. 376–81.
9. S. Steuer, P. Villechaise, T.M. Pollock, and J. Cormier: *Mater. Sci. Eng. A*, 2015, vol. 645, pp. 109–15.
10. J. Miao, T.M. Pollock, and J. Wayne Jones: *Acta Mater.*, 2009, vol. 57, pp. 5964–74.
11. A. Cervellon, J. Cormier, F. Maugé, and Z. Hervier: *Int. J. Fatigue*, 2017, vol. 104, pp. 251–62.
12. A. Cervellon, J. Cormier, F. Maugé, Z. Hervier, and Y. Nadot: *Metall. Mater. Trans. A*, 2018, vol. 49A, pp. 3938–50.
13. A. Cervellon, S. Hémerly, P. Kürsteiner, B. Gault, P. Kontis, and J. Cormier: *Acta Mater.*, 2020, vol. 188, pp. 131–44.
14. L.M. Bortoluci Ormastroni, L. Mataveli Suave, A. Cervellon, P. Villechaise, and J. Cormier: *Int. J. Fatigue*, 2020, vol. 130, p. 105247.
15. L.M. Bortoluci Ormastroni, S. Utada, J. Rame, L. Mataveli Suave, K. Kawagishi, H. Harada, P. Villechaise, and J. Cormier: in *Proceedings of the International Symposium on Superalloys 2020*, S. Tin, M. Hardy, J. Clews, J. Cormier, Q. Feng, J. Marcin, C. O’Brien, and A. Suzuki, eds., Springer US, Seven Springs, PA, USA, 2020, pp. 341–51.
16. J.Z. Yi, C.J. Torbet, Q. Feng, T.M. Pollock, and J.W. Jones: *Mater. Sci. Eng. A*, 2007, vol. 443, pp. 142–49.
17. Z. Zhao, Q. Li, F. Zhang, W. Xu, and B. Chen: *Int. J. Fatigue*.
18. N.L. Loh and K.Y. Sia: *J. Mater. Process. Tech.*, 1992, vol. 30, pp. 45–65.
19. H.V. Atkinson and S. Davies: *Metall. Mater. Trans. A*, 2000, vol. 31A, pp. 2981–3000.
20. A.I. Epishin, T. Link, B. Fedelich, I.L. Svetlov, and E.R. Golubovskiy: *MATEC Web Conf.*, 2014, vol. 14, p. 08003.
21. R.O. Ritchie, B.L. Boyce, J.P. Campbell, O. Roder, A.W. Thompson, and W.W. Milligan: *Int. J. Fatigue*, 1999, vol. 21, pp. 653–62.
22. B. Ruttert, I. Lopez-Galilea, and W. Theisen: in *International Symposium on Superalloys*, S. Tin, M. Hardy, J. Clews, J. Cormier, Q. Feng, J. Marcin, C. O’Brien, and A. Suzuki, eds., TMS (The Minerals, Metals & Materials Society), Palm Springs, 2020, pp. 391–407.
23. A. Cervellon, J.Z. Yi, F. Corpacci, Z. Hervier, J. Rigney, P.K. Wright, C.J. Torbet, J. Cormier, J.W. Jones, and T.M. Pollock: in *Proceedings of the International Symposium on Superalloys 2020*, S. Tin, M. Hardy, J. Clews, J. Cormier, Q. Feng, J. Marcin, C.

- O'Brien, and A. Suzuki, eds., Springer US, Seven Springs, PA, USA, 2020, pp. 185–95.
24. J.B. Wahl and K. Harris: in *Proceedings of International Symposium on Superalloys 2016*, M.C. Hardy, E. Huron, U. Glatzel, B. Griffin, B. Lewis, C. Rae, V. Seetharaman, and S. Tin, eds., Springer US, Seven Springs, PA, USA, 2016, pp. 25–33.
 25. A.B. Parsa, P. Wollgramm, H. Buck, C. Somsen, A. Kostka, I. Povstugar, P.P. Choi, D. Raabe, A. Dlouhy, J. Müller, E. Spiecker, K. Demtroder, J. Schreuer, K. Neuking, and G. Eggeler: *Adv. Eng. Mater.*, 2015, vol. 17, pp. 216–30.
 26. B. Rutttert, D. Bürger, L.M. Roncery, A.B. Parsa, P. Wollgramm, G. Eggeler, and W. Theisen: *Mater. Des.*, 2017, vol. 134, pp. 418–25.
 27. B. Rutttert, C. Meid, L. Mujica Roncery, I. Lopez-Galilea, M. Bartsch, and W. Theisen: *Scr. Mater.*, 2018, vol. 155, pp. 139–43.
 28. L. Mujica Roncery, I. Lopez-Galilea, B. Rutttert, D. Bürger, P. Wollgramm, G. Eggeler, and W. Theisen: *Adv. Eng. Mater.*, 2016, vol. 18, pp. 1381–87.
 29. L. Mujica Roncery, I. Lopez-Galilea, B. Rutttert, S. Huth, and W. Theisen: *Mater. Des.*, 2016, vol. 97, pp. 544–52.
 30. A. Cervellon: PhD Thesis - Ecole Nationale Supérieure de Mécanique et d'Aérotechnique (ISAE-ENSM), Poitiers, France. <http://theses.fr/2018ESMA0009>, 2018.
 31. S. Utada, L.M. Bortoluci Ormastroni, J. Rame, P. Villechaise, and J. Cormier: *Int. J. Fatigue*, 2021, vol. 148, p. 106224.
 32. A. Cervellon, L.M. Bortoluci Ormastroni, Z. Hervier, T.M. Pollock, F. Pedraza, and J. Cormier: *Int. J. Fatigue*, 2021, vol. 142, p. 105962.
 33. L.M. Bortoluci Ormastroni, I. Lopez-Galilea, J. Pistor, B. Rutttert, C. Körner, W. Theisen, P. Villechaise, F. Pedraza, and J. Cormier: *Addit. Manuf.*, 2022, vol. 54, p. 102759.
 34. C.L. Brundidge and T.M. Pollock: in *Proceedings of International Symposium on Superalloys 2012*, E.S. Huron, R.C. Reed, M.C. Hardy, M.J. Mills, R.E. Montero, P. Portella, and J. Telesman, eds., Springer US, Seven Springs, PA, USA, 2012, pp. 379–85.
 35. Y. Furuya, K. Kobayashi, M. Hayakawa, M. Sakamoto, Y. Koizumi, and H. Harada: *Mater. Lett.*, 2012, vol. 69, pp. 1–3.
 36. M.T. Kim, S.Y. Chang, and J.B. Won: *Mater. Sci. Eng. A*, 2006, vol. 441, pp. 126–34.
 37. G. Appa Rao, M. Srinivas, and D.S. Sarma: *Mater. Sci. Eng. A*, 2004, vol. 383, pp. 201–12.
 38. G.A. Rao, M. Kumar, M. Srinivas, and D.S. Sarma: *Mater. Sci. Eng. A*, 2003, vol. 355, pp. 114–25.
 39. A. Epishin, B. Fedelich, T. Link, T. Feldmann, and I.L. Svetlov: *Mater. Sci. Eng. A*, 2013, vol. 586, pp. 342–49.
 40. I. Lopez-Galilea, S. Huth, and W. Theisen: *MATEC Web Conf.*, 2014, vol. 14, p. 13009.
 41. M.S.A. Karunaratne, D.C. Cox, P. Carter, and R.C. Reed: in *Proceedings of International Symposium on Superalloys 2000*, T.M. Pollock, R.D. Kissinger, R.R. Bowman, K.A. Green, M. McLean, S. Olson, and J.J. Schirra, eds., TMS (The Minerals, Metals & Materials Society), Seven Springs, PA, USA, 2000, pp. 263–72.
 42. N. Saunders and A.P. Miodownik: *CALPHAD (Calculation of Phase Diagrams): A Comprehensive Guide*, First., Pergamon, 1998.
 43. X.G. Zheng, Y.N. Shi, and L.H. Lou: *J. Mater. Sci. Technol.*, 2015, vol. 31, pp. 1151–57.
 44. S. Steuer, Z. Hervier, S. Thabart, C. Castaing, T.M. Pollock, and J. Cormier: *Mater. Sci. Eng. A*, 2014, vol. 601, pp. 145–52.
 45. R.J. Morrissey and P.J. Golden: *Int. J. Fatigue*, 2007, vol. 29, pp. 2079–84.
 46. M. Zhao, T. Wu, Z. Zhao, L. Liu, G. Luo, and W. Chen: *Appl. Sci.*, 2020, vol. 10, pp. 1–4.
 47. S. Stanzl-Tschegg: *Int. J. Fatigue*, 2014, vol. 60, pp. 2–17.
 48. M. Lamm and R.F. Singer: *Metall. Mater. Trans. A*, 2007, vol. 38, pp. 1177–83.
 49. M.R.G. Prasad, S. Gao, N. Vajragupta, and A. Hartmaier: *Crystals*, 2020, vol. 10, pp. 1–5.
 50. A. Harte, M. Atkinson, M. Preuss, and J. Quinta da Fonseca: *Acta Mater.*, 2020, vol. 195, pp. 555–70.
 51. B. Rutttert, O. Horst, I. Lopez-galilea, D. Langenkämper, A. Kostka, C. Somsen, J.V. Goerler, M.A. Ali, O. Shchyglo, I. Steinbach, G. Eggeler, and W. Theisen: *Metall. Mater. Trans. A*, 2018, vol. 49A, pp. 4262–73.
 52. R. Xu: *Mater. Lett.*, 2005, vol. 59, pp. 2818–20.
 53. Y. Zhou, Z. Zhang, Z. Zhao, and Q. Zhong: *J. Mater. Eng. Perform.*, 2013, vol. 22, pp. 215–22.
 54. Y. Zhang, L. Liu, T. Huang, Q. Yue, D. Sun, J. Zhang, W. Yang, H. Su, and H. Fu: *J. Alloys Compd.*, 2017, vol. 723, pp. 922–29.
 55. I. Lopez-Galilea, S. Huth, W. Theisen, T. Fockenbergh, and S. Chakraborty: *J. Mater. Sci.*, 2013, vol. 48, pp. 348–58.
 56. A. Sato, H. Harada, T. Yokokawa, T. Murakumo, Y. Koizumi, T. Kobayashi, and H. Imai: *Scr. Mater.*, 2006, vol. 54, pp. 1679–84.
 57. C.M.F. Rae, M.S. Hook, and R.C. Reed: *Mater. Sci. Eng. A*, 2005, vol. 396, pp. 231–39.
 58. M. Simonetti and P. Caron: *Mater. Sci. Eng. A*, 1998, vol. 254, pp. 1–2.

Publisher's Note Springer Nature remains neutral with regard to jurisdictional claims in published maps and institutional affiliations.

Springer Nature or its licensor (e.g. a society or other partner) holds exclusive rights to this article under a publishing agreement with the author(s) or other rightsholder(s); author self-archiving of the accepted manuscript version of this article is solely governed by the terms of such publishing agreement and applicable law.